Engineering Transactions, **66**(4): 391–412, 2018, doi: 10.24423/EngTrans.723.20180924
Polish Academy of Sciences • Institute of Fundamental Technological Research (IPPT PAN)
Université de Lorraine • Poznan University of Technology

Research Paper

A Mechanical Model of Heart Valves with Chordae for in Silico Real-Time Computations and Cardiac Surgery Planning

Gediminas GAIDULIS[1)], Rimantas KAČIANAUSKAS[1)]
Natalya KIZILOVA[2)], Yury ROMASHOV[3)]

[1)] *Vilnius Gediminas Technical University*
Institute of Mechanical Sciences
J. Basanavičiaus st., 28, 03-109 Vilnius, Lithuania
e-mail: {gediminas.gaidulis, rimantas.kacianauskas}@vgtu.lt

[2)] *Warsaw University of Technology*
Institute of Aeronautics and Applied Mechanics
Nowowiejska 24, 00-665 Warsaw, Poland
e-mail: n.kizilova@gmail.com

[3)] *Kharkov National Polytechnic University "KPI"*
Kyrpichova st., 21, 61-000 Kharkov, Ukraine
e-mail: yu.v.romashov@gmail.com

In this paper, a two-dimensional (2D) model of the dynamics of mitral valve with chordae is developed based on in vivo data of the periodical motion of the valve leaflets digitized from the ultrasound imaging. The chordae are considered as viscoelastic springs described by the five-element rheological model. The model allows fast numerical computations of forces in the chordae and leaflets at different locations of the chordae of a different order. It can be used in real-time computations of the patient-specific geometry for optimal surgery planning when the mitral valve insufficiency is associated with broken chordae, and neochordae implantation is needed.

Key words: mitral valve biomechanics; neochordae; viscoelastic tissue; in silico surgery planning.

1. Introduction

Development of mechanical models of biological tissues and numerical estimation of their strength and durability has become an important component of surgery planning based on patient-specific geometry [1–3]. The models of

the coronary and carotid stenosis, brain and aortic aneurysms, heart chambers and valves have been developed based on three-dimensional (3D) geometry restored from computed tomography (CT) data [2, 3]. The mitral valve (MV) is located between the left atrium and ventricle; it consists of two flexible leaflets composed of inextensible viscoelastic material (Figs. 1a, b). The leaflets are open during the atrial systole when the pressure is greater in the atrium and closed in ventricular systole when the blood pressure becomes greater in the ventricle. The valve provides unidirectional blood flow from the atrium (A in Fig. 1a) into the ventricle (V in Fig. 1a) during the systole because the reverse movement of the leaflets is restricted by a family of threads (chordae) connecting the surfaces of the leaflets to the papillary muscles (PM) in the ventricles. If the chordae are ruptured or over distended, MV is not closed properly when the heart pumps blood out, and the mitral insufficiency develops [4]. Then cardiac surgery with neochordae implanting is obligatory. The age-related and pathological changes of the leaflets can affect its mechanical integrity, which may result in incomplete closure (MV regurgitation) which is the second most common valvular problem among elderly persons in Europe. The bottom view of the MV with incomplete closure of the two leaflets can be restored from 3D transesophageal ultrasound (US) examination. Surgical interventions are based on polytetrafluoroethylene (PTFE) neochordae reconstruction that normalizes the valve biomechanics. Unfortunately, in ∼40–50% of cases the surgery is unsuccessful and the remaining intact chordae become over distended or ruptured due to high stresses experienced by them or trauma produced by stretched PTFE strings.

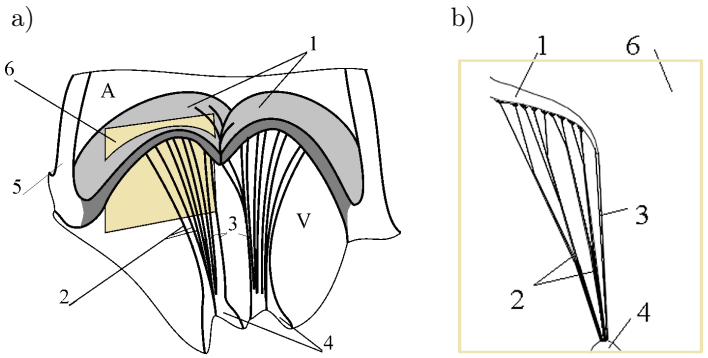

Fig. 1. 3D (a) and 2D (b) schemas of the mitral MV construction: 1 – leaflets, 2 – basal (secondary) chordae, 3 – marginal (primary) chordae, 4 – papillary muscle, 5 – heart walls, 6 – cross-sectional plane, A – left atrium, V – left ventricle.

Since the heart with its valves and chordae possesses very complex geometry and biomechanics, the 2D and 3D modeling of its dynamics, computations of the stress-strain state, biomechanical interpretation of the numerical results, and *in silico* planning and quantitative estimation of the outcome of surgery

are of great importance. The 2D geometry of the heart valves can be obtained from heart ultrasound (HUS) examination that gives us real-time imaging of the periodic heart contraction and leaflets' displacements, though the chordae are hardly visible there [5]. The HUS side view (Fig. 2a) gives a dynamic image of the heart chambers, PM and leaflets, which is suitable for the 2D modeling. The positions of the leaflets can be digitized (Fig. 2b) and used for the modeling purposes. In this case, the 2D model corresponds to some cross-sectional plane (6 in Figs. 1a, b) with a slice of the leaflet and the set of chordae connected to it. When the neochordae surgery is conducted on the stopped heart, the *in situ* geometry of the chordae can be directly estimated and introduced into the model, provided the computation times are reasonably short to simulate the results of possible different locations of the neochordae.

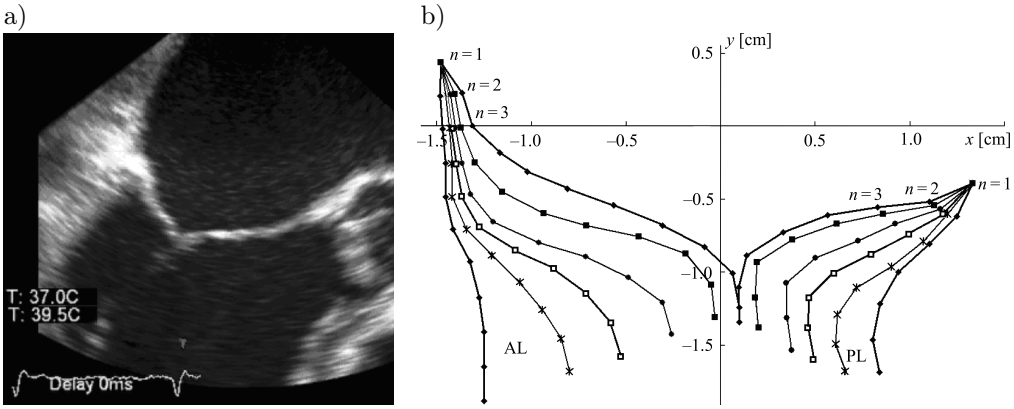

FIG. 2. HUS image (a) and digitized movements of the MV leaflets (b).

The multi-row CT produces a series of 2D slices of the heart structures taken at the moments when the valve is closed. The 3D structure can be automatically restored from the large set of 2D images [6]. Since each measurement gives a quite thin set of slices, for instance, $h = 0.7$ mm for 64-row CT, a long series of consequent measurements along the heart axis is needed to obtain the whole heart geometry ($H = 10$–14 cm). Therefore, the reconstructed 3D structure consists of 2D images taken at different heart contractions. The chordae remain invisible again but some suggestions on their location can be formulated because, at the sites of fastening of the chordae to the leaflets, the corresponding leaflet area is slightly thicker (Fig. 1b). Sometimes thick basal ($d = 2$–3 mm) chordae connected to the leaflet surface could be visible, while the marginal (0.5–1 mm) chordae fastened to the edge of the leaflet were invisible. The basal chordae often exhibit branched structures (Fig. 2b). Detailed anatomical studies on human hearts revealed at least two basal chordae in 100% of anterior leaflets and 63.6%

of posterior leaflets [7]. Individual geometry and location of the basal chordae influence severity of the valve insufficiency [8].

In the past, different 2D finite element method (FEM) models have been built and tested without the chordae [9], and with a set of single chordae attached along the edges of the leaflets only [10]. The FEM computations are time-consuming and geometry-dependent. Therefore, more elaborate numerical computations are needed to estimate the influence of different characteristics of the normal or affected patient-specific geometry and material parameters on the stress-strain state of the system modelled.

Special comparative analysis of the mass-spring (MS) and FEM valve models of the heart leaflets revealed that the MS model is less accurate but approximately an order of magnitude faster than the FEM models [11]. Contrary to FEM, the MS model does not have direct mechanism to control shear stresses in the soft tissues. However, because the shear loading of the pressurized leaflets is much smaller than the normal forces experienced by them, the MS model approximates the deformations with small errors despite complex biomechanical properties of the leaflets [11].

The 3D geometry of the MV obtained from CT is static and corresponds to the closed valve with stretched chordae. In that way, introducing realistic dynamics of the leaflet motion into FEM models can be done using special experimental techniques. In [12], a set of radiopaque markers were attached at the areas of connection between a chorda and the leaflet surface. Location of the markers was detected and used for development of the dynamical 3D model. The chordae were modelled as tension-only elements radiating from the PM tips. The model was used for inverse problem solution, i.e., determination of the mechanical forces from known dynamic trajectories, and rough estimation of material properties of the mitral MV tissues.

The brief literature review demonstrates a set of different problems in patient-specific modeling of the MV dynamics especially for fast real-time numerical computations and analysis of the stress distribution in the tissues, especially for surgery planning and decision making during the surgery on a stopped or unstopped heart. Reasonable simplification of the model is crucial for solving the problem in PBARL. It is SIEMENS software for digital simulation solutions by bar elements in NASTRAN. Moreover, the sensitivity of the model to individual rheological parameters of the tissues and its ability to give reliable quantitative estimations is of great importance.

In this paper, a reasonable mechanical model of the MV leaflets dynamically interacting with blood flow, PM and a set of chords is proposed. The very first computational results have been recently reported [13, 14]. FEM computations are time-consuming, and a special CFD team is needed to conduct them. In contrast, the modeling and approach stated below can be used for fast pre-

liminary analysis and planning the surgery on the restoration of the ruptured or over distended chordae. Our approach allows further automatic computations on a corrected model when the heart is stopped, and new details on patient-specific geometry, diameters of chordae, thickness and rigidity of the leaflets and other soft tissues become known. The model can be used by surgeons themselves, as it comes with a user friendly interface.

2. Materials and methods

For this study, the MV dynamics were recorded by HUS (side view) on healthy volunteers and patients of Vilnius University Hospital Santariškių Klinikos, Cardiosurgery Department with different types of MV regurgitation. The consequent images sampled at the time interval $\Delta t = 0.07$ s were digitized, and locations of the anterior (AL, longer one) and posterior (PL, shorter one) MV leaflets were determined. Both leaflets were considered as k-link flexible threads which segments $k = 1, 2, \ldots, k_{\mathrm{AL}}$ and $k = 1, 2, \ldots, k_{\mathrm{PL}}$. The lengths of the segments were chosen as equal. An example of the dynamics of the AL and PL of a healthy individual is presented in Fig. 3. The leaflets exhibit complex trajectories in the (x, y) coordinate system. The points of attachments of the AL and PL to the heart walls also demonstrate quite complex patient-specific trajectories that typically have double-8 shapes (curves 1, 2 in Fig. 4). The initial part of the trajectories starts with a short linear displacement between $t = 0$ and $t = t_1$, and for the example given in Fig. 3 $t_1 = 0.14$ s (Fig. 4). Then, the heart starts a reverse movement and reaches its peak at $t = t_2$ corresponding to early dias-

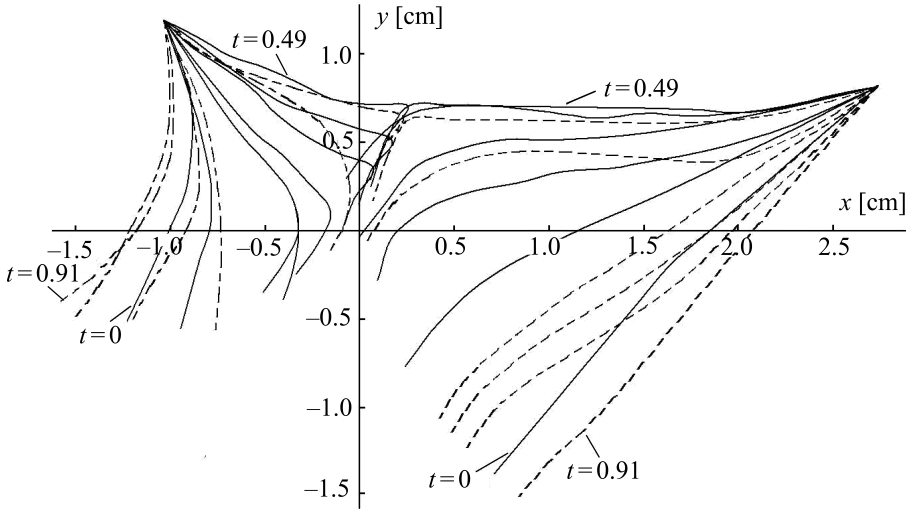

Fig. 3. Consequent locations of the AL (right side) and PL (left side) during the heart contraction from $t = 0$ to $t = 0.91$ s.

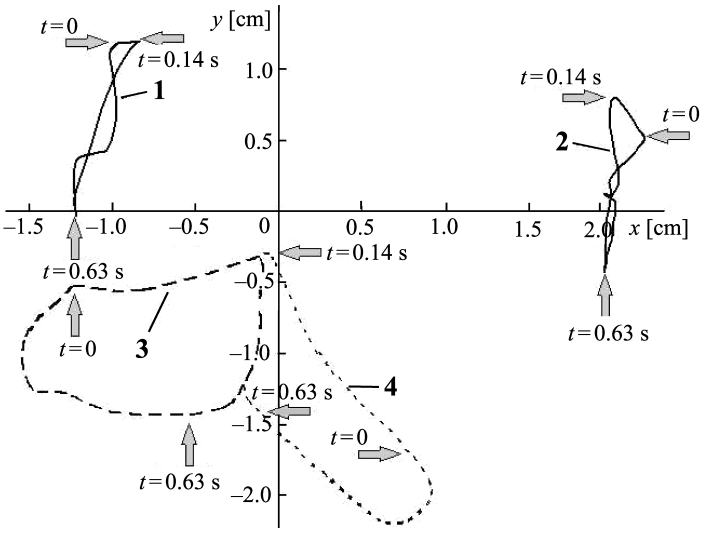

FIG. 4. Trajectories of the basis (1, 2) and edges (3, 4) of AL (2, 4) and PL (1, 3) in the (x, y) coordinates.

tole; in the case considered in Fig. 3 $t_2 = 0.63$ s (Fig. 4). At $t > t_2$, the direction of the heart motion is reversed again until it returns into the initial state.

The free edges of the leaflets demonstrate the closed loop trajectories almost without self- cross-sections (curves 3, 4 in Fig. 4). The two loops have a common path of their trajectories at $t_1 < t < t_2$, which corresponds to the closed valve when the leaflets are moving in a tight contact that is clearly visible in the curves 3 and 4 (Fig. 4). Those curves are the result of the superposition of the movements of the leaflets generated by the blood flow streams passing into the ventricle and out of it, and the displacements of the (x, y) coordinate system together with moving heart walls.

Subtraction of the coordinate system movements (i.e., trajectories of the basis, curves 1 and 2 in Fig. 4) from the trajectories of the edges (curves 3 and 4 in Fig. 4) gives trajectories of the relative movements of the valves in the (x, y) coordinates which become more regulate and could be easily approximated by exponent functions $y_j = b_j \exp(a_j x_j)$. The results of subtraction (curves 1 and 2) in comparison to visible trajectories (curves 3 and 4) are presented in Fig. 5 for the $n = 8$ point in each multilink model counting from the base of both AL and PL (see numeration in Fig. 2b). The curves 3 and 4 represent the actual repeated displacement of the node. Being supplied by in vivo measurements of the blood pressure in the left side of the heart, the curves may serve for computations of the energy used for a cycle of the valve motion. That type of curves is prevalent in heart biomechanics and advanced medical diagnostics based on the typical shapes of the displacement curves in normalcy and pathology.

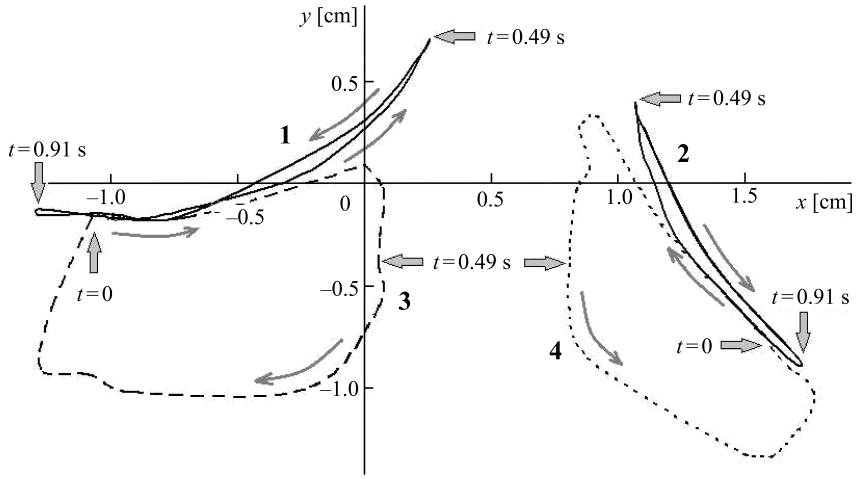

FIG. 5. Trajectories of the relative movement of the basis (1, 2) and edges (3,4) of AL (2, 4) and PL (1, 3) with own heart trajectories subtracted.

Next, the displacements of the nodes of AL and PL in each 2D (HUS) measured case were computed. A sample of the displacement

$$d_n(t_k) = \sqrt{(x_{nk} - x_{n0})^2 + (y_{nk} - y_{n0})^2}$$

relative to initial location (at $t = 0$) computed for the nodes $n = 0, ..., 9$ of the PL is presented in Fig. 6a. The displacements were computed on the 2D measured data such as curves 3 and 4 in Figs. 4 and 5, without subtraction of the heart movement. The computed curves were compared to the 3D measurements of the displacement field of a set of radiopaque markers attached to the MV leaflets of ovarian hearts [12]. In Fig. 6b, the distribution of the radiopaque markers is presented. In [12] the 3D displacement fields were computed by averaging data from the measured markers over the entire surface of the leaflets. Comparison of our 2D computed data to the distribution of the 3D displacement fields along the virtual 2D slices (marked in Fig. 6b by elongated rectangles) showed very good qualitative correspondence (Fig. 6c). The quantitative differences are explained by different dimensions, heart rates, blood pressure and valve biomechanics in sheep and humans.

In this study, ten mitral valves were analysed, and the dependencies $y_j = b_j \exp(a_j x_j)$ were obtained for five healthy individuals, while the patients with different MV insufficiencies demonstrated more complex irregular dynamics of their (x, y) trajectories. This implies that the simplified dynamical description of the healthy MV can be described by a series of exponential type trajectories for each joint of the multilink model of the MV leaflets. It enables generation

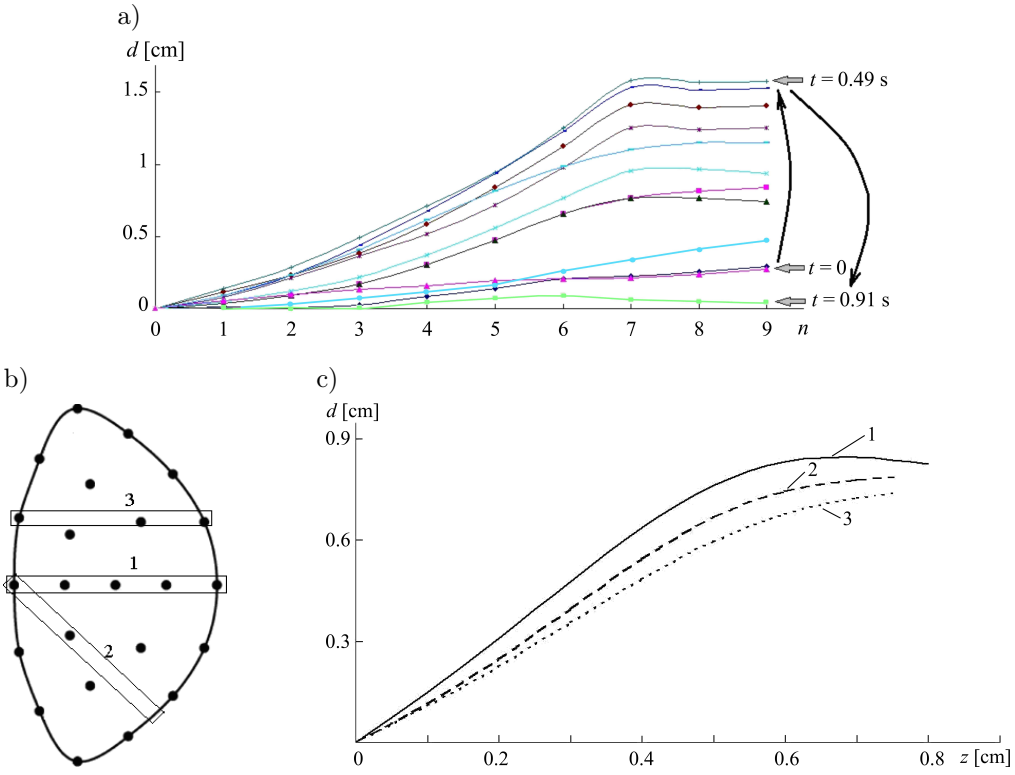

FIG. 6. Displacements of $n = 1, \ldots, 6$ nodes of the PL model (a) and location of the radiopaque markers on the PL [12] (b).

of realistic 3D movements of the valve surface, without experimental technique described in [12], by using the non-invasive HUS data only, which is confirmed by the qualitative correspondence of the HUS-based measurements and realistic 3D MV movements measured *in vivo*. A more detailed recommendation may be given by evaluation of data from a representative group of each type of the MV insufficiency.

3. Mathematical formulation of the chordae dynamics

The considered complex biomechanical system is studied here as a holonomic mechanical system with some finite number of degrees of freedom (DOF) described by the generalized coordinates q_p, $p = 1, 2, \ldots$ Then its movement can be presented in the form of the Lagrange's equations of the second kind:

$$\frac{\mathrm{d}}{\mathrm{d}t}\frac{\partial L}{\partial \dot{q}_p} - \frac{\partial L}{\partial q_p} = Q_p + R_p, \tag{3.1}$$

where L is the Lagrange function for the heart muscle, Q_p are generalized forces produced by the action of the moving chordae on the valves, and R_p are generalized forces produced by other factors.

As it follows from (3.1), the modeling of mechanical behaviour of the chordae is reduced to determining the generalized forces Q_p and R_p, $p = 1, 2, \ldots$ The patient-specific geometry of the chordae will be described by the index $s = 1, 2, \ldots$ (Fig. 7a). The chordae system is presented by both single and branched chords. Then it is assumed the chorda s has $\mu^{(s)}$ ends numerated as $i = 1, 2, \ldots, \mu^{(s)}$; location of each chord is determined by the position vectors $\boldsymbol{\rho}_i^{(s)}$ (Fig. 7b). When the valve is open, the chordae are not stretched and slack, which means that their interaction with the leaflets is determined by the main force vector directed along the corresponding rectilinear segment, while the net moment of force in the attachment points ($n = 1, 2, 3, \ldots$ in Fig. 2b) is zero. Let us denote as $\boldsymbol{\Phi}_i^{(s)}$ the main force vectors acting onto the valve and applied in the nodes $i = 1, 2, \ldots, \mu^{(s)}$ (Fig. 7b). As a sample of the complex structures, the branched chord is considered (solid linens in Fig. 7b). Now the generalized forces Q_p, $p = 1, 2, \ldots$ can be calculated from the virtual work δA produced by the forces $\boldsymbol{\Phi}_i^{(s)}$, $i = 1, 2, \ldots, \mu^{(s)}$ in the chordae $s = 1, 2, \ldots$ attached to both leaflets

$$\delta A = \sum_{s=1,2,\ldots} \sum_{i=1}^{\mu^{(s)}} \boldsymbol{\Phi}_i^{(s)} \cdot \delta \boldsymbol{\rho}_i^{(s)}, \tag{3.2}$$

where $\delta \boldsymbol{\rho}_i^{(s)}$ are virtual displacements of the chordae ends.

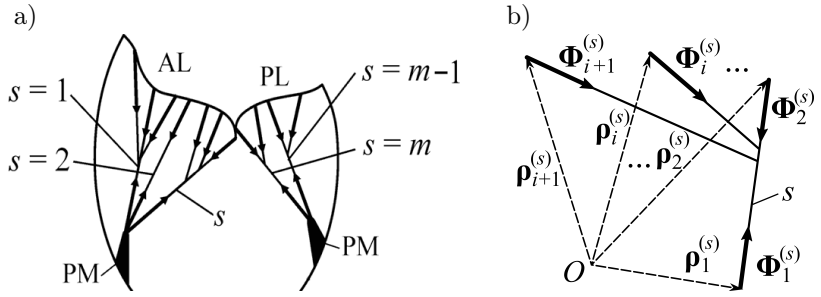

FIG. 7. A sample of individual geometry of the chordae (a) and the forces produced by them at the leaflet and papillary muscle (b); $s = 1, 2, \ldots$ are ordinal numbers of the chordae.

Since locations of the basal ends of the chordae coincide with contracting heart tissues, the position vectors $\boldsymbol{\rho}_i^{(s)}$ could be defined via the generalized coordinates q_p assuming the constraints between the chordae and tissues are stationary: $\boldsymbol{\rho}_i^{(s)} = \boldsymbol{\rho}_i^{(s)}(q_1, q_2, \ldots, q_p, \ldots)$, which is natural for the incompressible fibrous

tissues. Then after some transformations of Eq. (3.2) the generalized forces can be obtained in the form

$$\widehat{Q}_p = \sum_{s=1,2,\ldots} \sum_{i=1}^{\mu^{(s)}} \mathbf{\Phi}_i^{(s)} \cdot \frac{\partial \boldsymbol{\rho}_i^{(s)}}{\partial q_p}. \tag{3.3}$$

As it is stated by (3.3), for computations of Q_p the expressions for $\mathbf{\Phi}_i^{(s)}$ are needed. Those expressions are determined by known (measured) movements of the leaflets and deformation of the chordae.

3.1. Modeling of chords as viscoelastic threads

Let us consider the single chordae as elastic threads with Young's modulus proper for elastic materials and biological tissues ($E = 10^5$–10^8 Pa) and zero bending rigidity. Such chordae can sustain quite high stresses produced by the blood pressure in the heart chambers but become easily bent and slack when the valve is open. The current length of the thread in the stretched state can be described by the distance between its ends A and B determined by their positional vectors $\mathbf{r}_A$ and $\mathbf{r}_B$ (Fig. 3). Then the length and the elongation rate of the thread are

$$\begin{cases} l = \sqrt{(\mathbf{r}_B - \mathbf{r}_A) \cdot (\mathbf{r}_B - \mathbf{r}_A)}, \\ \dot{l} = (\mathbf{r}_B - \mathbf{r}_A) \cdot (\dot{\mathbf{r}}_B - \dot{\mathbf{r}}_A) \Big/ \sqrt{(\mathbf{r}_B - \mathbf{r}_A) \cdot (\mathbf{r}_B - \mathbf{r}_A)}. \end{cases} \tag{3.4}$$

Together with the geometric constraints (3.4), we assume the internal forces acting at any infinitesimal segment SS' ($dl \ll |AB|$) of the thread on its cross-sections S and S' are equivalent to the main force vectors $\mathbf{F}$ and $\mathbf{F}'$ directed along the thread in its current position where $\mathbf{F}' = -\mathbf{F}$ (Fig. 8). The forces $\mathbf{F}_A$ and $\mathbf{F}_B$ at the ends A and B of the thread satisfy the same condition $\mathbf{F}_B = -\mathbf{F}_A$. Due to zero bending rigidity of the threads, the forces $\mathbf{F}$, $\mathbf{F}'$, $\mathbf{F}_A$, $\mathbf{F}_B$ are purely stretching ones. The main vectors of internal forces have the same value $F = |\mathbf{F}|$ in each cross-section of the stretched thread, which is a tensile force.

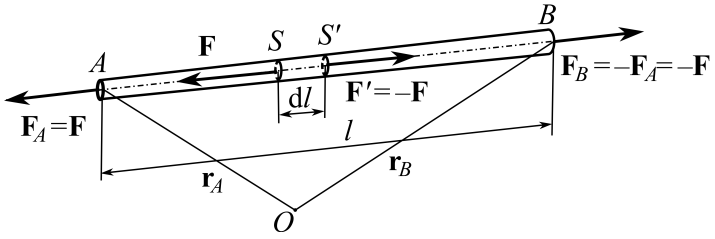

FIG. 8. A stretched thread and its internal forces.

The mechanical behaviour of the viscoelastic thread is described by the dependence

$$F = F\left(l - l_0, \dot{l}\right), \tag{3.5}$$

where l_0 is its length in the unloaded (unstrained) state.

As it follows from (3.4) and (3.5), the tensile force is the function of the initial length, current coordinates and elongation rate

$$F = F\left(\mathbf{r}_A, \mathbf{r}_B, \dot{\mathbf{r}}_A, \dot{\mathbf{r}}_B; l_0\right). \tag{3.6}$$

Note that Eq. (3.6) is a nonlinear function even when the linear viscoelasticity model is accepted for the thread material.

3.2. Modeling the mechanical behaviour of the rectilinear threads

In the simplest case, the chorda possesses two ends attached to the PM and the leaflet accordingly (e.g., the chorda $s = 2$ in Fig. 7a) and $\mu^{(s)} = 2$ (Fig. 9a). The mechanical behaviour of such chorda is determined by the law (3.5) only. Indeed, in the case $\mu^{(s)} = 2$ the forces produced by the chorda s at the leaflet and PM are functions of its tensile force (Fig. 9a):

$$\begin{cases} \boldsymbol{\Phi}_1^{(s)} = \Phi^{(s)}\left(\boldsymbol{\rho}_1, \boldsymbol{\rho}_2, \dot{\boldsymbol{\rho}}_1, \dot{\boldsymbol{\rho}}_2; l_0^{(s)}\right) \dfrac{\boldsymbol{\rho}_2 - \boldsymbol{\rho}_1}{\sqrt{(\boldsymbol{\rho}_2 - \boldsymbol{\rho}_1) \cdot (\boldsymbol{\rho}_2 - \boldsymbol{\rho}_1)}}, \\ \boldsymbol{\Phi}_2^{(s)} = -\boldsymbol{\Phi}_1^{(s)}, \end{cases} \tag{3.7}$$

where $\Phi^{(s)}\left(\boldsymbol{\rho}_1, \boldsymbol{\rho}_2, \dot{\boldsymbol{\rho}}_1, \dot{\boldsymbol{\rho}}_2; l_0^{(s)}\right)$ is the mechanical law for the chorda expressed in the form (3.6).

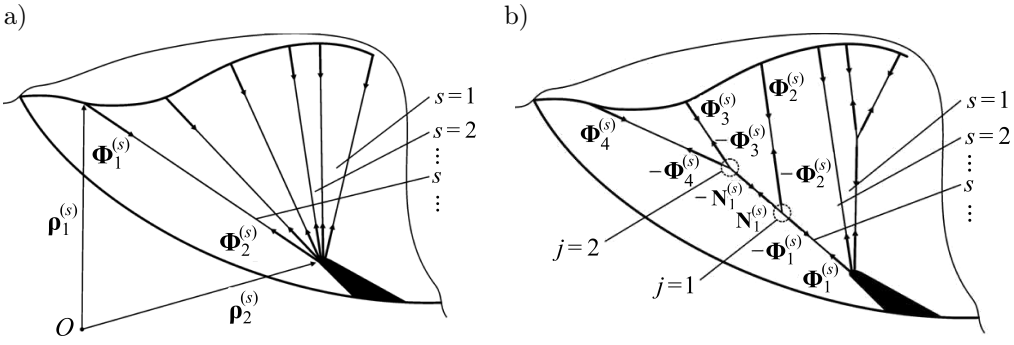

FIG. 9. A leaflet with a set of six rectilinear chordae (a) and with one rectilinear and two branched chordae (b).

The expressions (3.7) are needed for computations of the generalized forces Q_p by (3.3). When all the chordae are rectilinear (Fig. 9a), one can obtain the expressions (3.7) written for each chorda in the structure, which gives the system of nonlinear equations for determination of the generalized forces that may be solved numerically.

3.3. Modeling the mechanical behaviour of the branched threads

The branched chordae can be considered as a system of viscoelastic threads attached together at some nodes outside of the leaflets (Fig. 9b). The forces appearing in the nodes are directed along the stretched segments and obey Newton's third law. An example of the force distribution is presented in Fig. 9b for $\mu^{(s)} = 4$. In the internal segments attached to neither PM nor leaflet, the internal tensile forces $\mathbf{N}_1^{(s)}$ appear. In a general case, we have $m^{(s)}$ nodes determined by the position vectors $\mathbf{r}_j^{(s)}$ numerated by the index $j = 1, 2, \ldots, m^{(s)}$, as well as $\nu^{(s)}$ internal segments experiencing the tensile forces $\mathbf{N}_k^{(s)}$, $k = 1, 2, \ldots, \nu^{(s)}$.

Let us denote $J^{(s)}(i)$ as the ordinal number of the node connected to the end $i \in 1, 2, \ldots, \mu^{(s)}$ of the chorda s. Similarly, $J_1^{(s)}(k)$ and $J_2^{(s)}(k)$ are the ordinal numbers of the nodes of the chorda s, which are connected to the internal segment number $k \in 1, 2, \ldots, \nu^{(s)}$. $\mathbf{N}_k^{(s)}$ and $-\mathbf{N}_k^{(s)}$ are the forces acting in the nodes with numbers $J_1^{(s)}(k)$ and $J_2^{(s)}(k)$ accordingly. Then, the forces $\mathbf{\Phi}_i^{(s)}$, $i = 1, 2, \ldots, \mu^{(s)}$, and $\mathbf{N}_k^{(s)}$, $k = 1, 2, \ldots, \nu^{(s)}$, can be computed as follows:

$$\mathbf{\Phi}_i^{(s)} = \Phi_i^{(s)}\left(\boldsymbol{\rho}_i^{(s)}, \mathbf{r}_{J^{(s)}(i)}^{(s)}, \dot{\boldsymbol{\rho}}_i^{(s)}, \dot{\mathbf{r}}_{J^{(s)}(i)}^{(s)}; \lambda_{i0}^{(s)}\right) \cdot \frac{\boldsymbol{\rho}_i^{(s)} - \mathbf{r}_{J^{(s)}(i)}^{(s)}}{\sqrt{\left(\boldsymbol{\rho}_i^{(s)} - \mathbf{r}_{J^{(s)}(i)}^{(s)}\right) \cdot \left(\boldsymbol{\rho}_i^{(s)} - \mathbf{r}_{J^{(s)}(i)}^{(s)}\right)}}, \tag{3.8}$$

$$\mathbf{N}_k^{(s)} = N_k^{(s)}\left(\mathbf{r}_{J_1^{(s)}(k)}^{(s)}, \mathbf{r}_{J_2^{(s)}(k)}^{(s)}, \dot{\mathbf{r}}_{J_1^{(s)}(k)}^{(s)}, \dot{\mathbf{r}}_{J_2^{(s)}(k)}^{(s)}; l_{k0}^{(s)}\right) \cdot \frac{\mathbf{r}_{J_2^{(s)}(k)}^{(s)} - \mathbf{r}_{J_1^{(s)}(k)}^{(s)}}{\sqrt{\left(\mathbf{r}_{J_2^{(s)}(k)}^{(s)} - \mathbf{r}_{J_1^{(s)}(k)}^{(s)}\right) \cdot \left(\mathbf{r}_{J_2^{(s)}(k)}^{(s)} - \mathbf{r}_{J_1^{(s)}(k)}^{(s)}\right)}}, \tag{3.9}$$

where

$$\Phi_i^{(s)}\left(\boldsymbol{\rho}_i^{(s)}, \mathbf{r}_{J^{(s)}(i)}^{(s)}, \dot{\boldsymbol{\rho}}_i^{(s)}, \dot{\mathbf{r}}_{J^{(s)}(i)}^{(s)}; \lambda_{i0}^{(s)}\right) \quad \text{and} \quad \lambda_{i0}^{(s)}$$

are the dynamics law and initial undisturbed length of the corresponding marginal segment,

$$N_k^{(s)}\left(\mathbf{r}^{(s)}_{J_1^{(s)}(k)}, \mathbf{r}^{(s)}_{J_2^{(s)}(k)}, \dot{\mathbf{r}}^{(s)}_{J_1^{(s)}(k)}, \dot{\mathbf{r}}^{(s)}_{J_2^{(s)}(k)}; l^{(s)}_{k0}\right) \quad \text{and} \quad l^{(s)}_{i0}$$

are the dynamics law and initial undisturbed length of the corresponding internal segment.

Since $\boldsymbol{\rho}_i^{(s)} = \boldsymbol{\rho}_i^{(s)}(q_1, q_2, \ldots, q_p, \ldots)$, the forces (3.8) can be determined as

$$\boldsymbol{\Phi}_i^{(s)} = \boldsymbol{\Phi}_i^{(s)}\left(q_1, q_2, \ldots, \dot{q}_1, \dot{q}_2, \ldots, \mathbf{r}^{(s)}_{J^{(s)}(i)}, \dot{\mathbf{r}}^{(s)}_{J^{(s)}(i)}\right). \tag{3.10}$$

After substitution (3.10) into (3.3), one can obtain the following expressions for the generalized forces as functions of the generalized coordinates and their time derivatives:

$$Q_p = Q_p\left(q_1, q_2, \ldots, \dot{q}_1, \dot{q}_2, \ldots, \mathbf{r}_1^{(s)}, \ldots, \mathbf{r}_{m^{(s)}}^{(s)}, \dot{\mathbf{r}}_1^{(s)}, \ldots, \dot{\mathbf{r}}_{m^{(s)}}^{(s)}\right), \tag{3.11}$$

in which all the structures $s = 1, 2, \ldots$ are taken into account.

Since the chordae are thin threads and their mass is negligibly small in comparison to the heart tissues mass, the movement of the nodes is determined by Newton's second law in the matrix form:

$$\sum_{i=1}^{\mu^{(s)}} M_{ji}^{(s)} \boldsymbol{\Phi}_i^{(s)} + \sum_{i=1}^{\nu^{(s)}} \Lambda_{ji}^{(s)} \mathbf{N}_i^{(s)} = \mathbf{0}, \qquad j = 1, 2, \ldots, m^{(s)}, \tag{3.12}$$

where $M_{ji}^{(s)}$ and $\Lambda_{jk}^{(s)}$ are the matrices determined by the geometry of the branched chordae; when the fibers j and i are connected, the element located in the j-th row and i-th column is equal to one; otherwise it is zero.

Substituting (3.9), (3.10) into (3.12), we obtain the differential relationships which at known generalized coordinates $q_1, q_2, \ldots$ determined by the heart movement can be considered as differential equations for determination of the position vectors $\mathbf{r}_j^{(s)}$, $j = 1, 2, \ldots, m^{(s)}$, of the nodes. Therefore, the proposed mathematical model of heart biomechanics includes the Lagrange's Eq. (3.1) for the heart tissues, that, accounting for (3.11) are coupled and must be integrated together with differential equations for displacements of the nodes (3.8), (3.9), (3.12).

4. Analysis of mechanical behaviour of the branched elastic chord

For the model validation reasons let us assume the viscous forces are small in comparison to the elastic ones. Then (3.5) can be written as

$$F = F\left(l - l_0\right). \tag{4.1}$$

Accounting for (4.1), we may accept instead (3.8), (3.9) the following expressions:

$$
(4.2)\qquad \begin{cases} \mathbf{\Phi}_i^{(s)} = \Phi_i^{(s)}\left(\boldsymbol{\rho}_i^{(s)}, \mathbf{r}_{J^{(s)}(i)}^{(s)}; \lambda_{i0}^{(s)}\right) \dfrac{\boldsymbol{\rho}_i^{(s)} - \mathbf{r}_{J^{(s)}(i)}^{(s)}}{\sqrt{\left(\boldsymbol{\rho}_i^{(s)} - \mathbf{r}_{J^{(s)}(i)}^{(s)}\right)\cdot\left(\boldsymbol{\rho}_i^{(s)} - \mathbf{r}_{J^{(s)}(i)}^{(s)}\right)}}, \\ \mathbf{N}_k^{(s)} = N_k^{(s)}\left(\mathbf{r}_{J_1^{(s)}(k)}^{(s)}, \mathbf{r}_{J_2^{(s)}(k)}^{(s)}; l_{k0}^{(s)}\right) \\ \qquad\qquad \cdot \dfrac{\mathbf{r}_{J_2^{(s)}(k)}^{(s)} - \mathbf{r}_{J_1^{(s)}(k)}^{(s)}}{\sqrt{\left(\mathbf{r}_{J_2^{(s)}(k)}^{(s)} - \mathbf{r}_{J_1^{(s)}(k)}^{(s)}\right)\cdot\left(\mathbf{r}_{J_2^{(s)}(k)}^{(s)} - \mathbf{r}_{J_1^{(s)}(k)}^{(s)}\right)}}. \end{cases}
$$

For the linear elasticity, the law (4.1) and expression (4.2) have the form:

$$
(4.3)\qquad F = c\,(l - l_0)\,,
$$

$$
(4.4)\qquad \begin{cases} \mathbf{\Phi}_i^{(s)} = \gamma_i^{(s)}\left(\sqrt{\left(\boldsymbol{\rho}_i^{(s)} - \mathbf{r}_{J^{(s)}(i)}^{(s)}\right)\cdot\left(\boldsymbol{\rho}_i^{(s)} - \mathbf{r}_{J^{(s)}(i)}^{(s)}\right)} - \lambda_{i0}^{(s)}\right) \\ \qquad\qquad \cdot \dfrac{\boldsymbol{\rho}_i^{(s)} - \mathbf{r}_{J^{(s)}(i)}^{(s)}}{\sqrt{\left(\boldsymbol{\rho}_i^{(s)} - \mathbf{r}_{J^{(s)}(i)}^{(s)}\right)\cdot\left(\boldsymbol{\rho}_i^{(s)} - \mathbf{r}_{J^{(s)}(i)}^{(s)}\right)}}, \\ \mathbf{N}_k^{(s)} = c_k^{(s)}\left(\sqrt{\left(\mathbf{r}_{J_2^{(s)}(k)}^{(s)} - \mathbf{r}_{J_1^{(s)}(k)}^{(s)}\right)\cdot\left(\mathbf{r}_{J_2^{(s)}(k)}^{(s)} - \mathbf{r}_{J_1^{(s)}(k)}^{(s)}\right)} - l_{k0}^{(s)}\right) \\ \qquad\qquad \cdot \dfrac{\mathbf{r}_{J_2^{(s)}(k)}^{(s)} - \mathbf{r}_{J_1^{(s)}(k)}^{(s)}}{\sqrt{\left(\mathbf{r}_{J_2^{(s)}(k)}^{(s)} - \mathbf{r}_{J_1^{(s)}(k)}^{(s)}\right)\cdot\left(\mathbf{r}_{J_2^{(s)}(k)}^{(s)} - \mathbf{r}_{J_1^{(s)}(k)}^{(s)}\right)}}, \end{cases}
$$

where c is the rigidity coefficient for the thread, and $\gamma_i^{(s)}$ and $c_k^{(s)}$ are stiffness of the marginal and internal nodes of the branched chord accordingly.

Substituting (4.4) into (3.12), we obtain the mathematical model of the linear elastic weightless chorda. The model is presented as a system of non-linear algebraic equations for determination of locations of the nodes governed by the known movement of the leaflets.

Let us consider the mechanical behaviour of the branched chorda with one internal node (Fig. 10). In the case $\mu^{(s)} = 3$, $m^{(s)} = 1$, $\nu^{(s)} = 0$, $M_{ji}^{(s)} = \begin{pmatrix} -1 & -1 & -1 \end{pmatrix}$, and the expressions (4.4) have the form:

$$\mathbf{\Phi}_i^{(s)} = \frac{\gamma_i^{(s)}\left(\sqrt{\left(\xi_i^{(s)}-x_1^{(s)}\right)^2+\left(\eta_i^{(s)}-y_1^{(s)}\right)^2}-\lambda_{i0}^{(s)}\right)}{\sqrt{\left(\xi_i^{(s)}-x_1^{(s)}\right)^2+\left(\eta_i^{(s)}-y_1^{(s)}\right)^2}} \cdot\left(\left(\xi_i^{(s)}-x_1^{(s)}\right)\mathbf{i}+\left(\eta_i^{(s)}-y_1^{(s)}\right)\mathbf{j}\right), \tag{4.5}$$

where $\xi_i^{(s)}$ and $\eta_i^{(s)}$ are coordinates of the ends of the chorda, $(x_1^{(s)},\ y_1^{(s)})$ are coordinates of its nodes, $\mathbf{i}$ and $\mathbf{j}$ are unit vectors of the coordinates $(x,\ y)$.

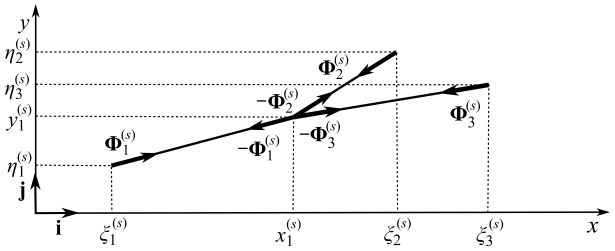

FIG. 10. An example of chorda with one branching mode.

Then from Eq. (4.5) one can obtain the nonlinear system of two equations for determination of the coordinates of the internal node $(x_1^{(s)},\ y_1^{(s)})$ in the form:

$$\begin{cases} -x_1^{(s)}\sum\limits_{i=1}^{3}\gamma_i^{(s)}+\sum\limits_{i=1}^{3}\gamma_i^{(s)}\xi_i^{(s)} = \sum\limits_{i=1}^{3}\dfrac{\gamma_i^{(s)}\lambda_{i0}^{(s)}\left(\xi_i^{(s)}-x_1^{(s)}\right)}{\sqrt{\left(\xi_i^{(s)}-x_1^{(s)}\right)^2+\left(\eta_i^{(s)}-y_1^{(s)}\right)^2}} \\ \qquad -2\dfrac{\gamma_1^{(s)}\lambda_{10}^{(s)}\left(\xi_1^{(s)}-x_1^{(s)}\right)}{\sqrt{\left(\xi_1^{(s)}-x_1^{(s)}\right)^2+\left(\eta_1^{(s)}-y_1^{(s)}\right)^2}}, \\ -y_1^{(s)}\sum\limits_{i=1}^{3}\gamma_i^{(s)}+\sum\limits_{i=1}^{3}\gamma_i^{(s)}\eta_i^{(s)} = \sum\limits_{i=1}^{3}\dfrac{\gamma_i^{(s)}\lambda_{i0}^{(s)}\left(\eta_i^{(s)}-y_1^{(s)}\right)}{\sqrt{\left(\xi_i^{(s)}-y_1^{(s)}\right)^2+\left(\eta_i^{(s)}-y_1^{(s)}\right)^2}} \\ \qquad -2\dfrac{\gamma_1^{(s)}\lambda_{10}^{(s)}\left(\eta_i^{(s)}-y_1^{(s)}\right)}{\sqrt{\left(\xi_1^{(s)}-x_1^{(s)}\right)^2+\left(\eta_1^{(s)}-y_1^{(s)}\right)^2}}, \end{cases} \tag{4.6}$$

where the coordinates of $(\xi_i^{(s)},\ \eta_i^{(s)})$ of the fastening points are known from the measurement data of the papillary muscle $(s=1)$ and two points of the leaflet $(s=2,\ 3)$ location at each instant time. Solution of (4.6) could be easily obtained

by using Newton's method with the initial approximation of the solution in the linear form

$$x_1^{(s)} = \frac{\sum_{i=1}^{3} \gamma_i^{(s)} \xi_i^{(s)}}{\sum_{i=1}^{3} \gamma_i^{(s)}}, \qquad y_1^{(s)} = \frac{\sum_{i=1}^{3} \gamma_i^{(s)} \eta_i^{(s)}}{\sum_{i=1}^{3} \gamma_i^{(s)}}.$$

The computation results may be validated by comparative analysis of the computed displacements of the nodes and the *in vivo* detected locations of the radiopaque beads introduced into the heart structures and nodes in acute experiment on animals [15] or direct measurements of the tensile stresses in the chordae/neochordae in the contracting heart *in situ* by the stress sensors [16].

5. Results and discussion

Despite the fact that the technical viscoelastic materials are characterized by single stress and strain relaxation times in the corresponding isometric and isotonic experiments, the biological soft tissues possess a set of stress and strain relaxations depending on the strain and stress values. In this study, the recent experimental data on rheological properties of the chordae in ovine hearts [17] was presented. The extensometer tensile tests were conducted on 18 fresh samples of the hearts. The measured data reveals nonlinear elasticity and correspondence to the five-element rheological model (Fig. 11a) with strain-dependent Young's modules (Fig. 11b). The elastic and viscous parameters used in this study are presented in Table 1.

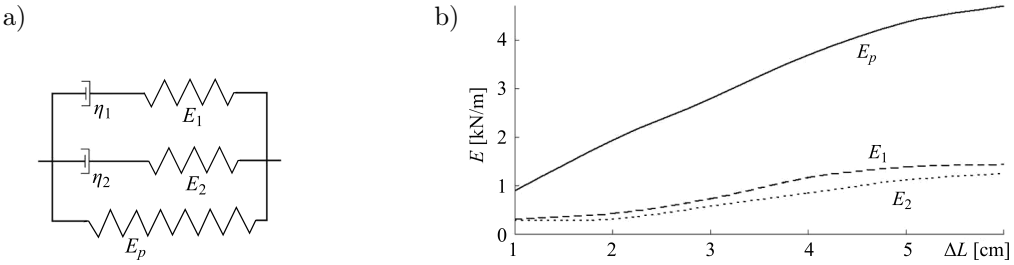

Fig. 11. Rheological model of the chorda's material.

The geometry of the mitral valve (dimensions, the location of the PM, valve dynamics) was taken for each case from the HUS records. The 10-link and 8-link models were assigned to the AL and PL accordingly. The chordae structure was generated according to statistical data on their location in human hearts [5, 7]. The primary chords were attached to the edges of the leaflets, and at least two branched basal chords were attached to the basal parts of the leaflets. An example of the structure is presented in Fig. 12a. Periodical displacements of

Table 1. Averaged measurement data for the material parameters of the rheological model (Fig. 11); ΔL is the absolute displacement of the chorda [17].

ΔL [mm]	E_p [kN/m]	E_1 [kN/m]	E_2 [kN/m]	η_1 [kN · s/m]	η_2 [kN · s/m]
1	0.92 ± 0.80	0.31 ± 0.25	0.28 ± 0.22	32.20 ± 23.78	1.84 ± 1.60
2	1.69 ± 1.40	0.49 ± 0.36	0.38 ± 0.27	55.84 ± 38.89	2.53 ± 1.90
3	2.50 ± 1.86	0.73 ± 0.51	0.58 ± 0.37	83.40 ± 58.61	3.75 ± 2.46
4	3.29 ± 2.11	0.97 ± 0.59	0.80 ± 0.44	109.93 ± 68.63	4.91 ± 2.61
5	4.07 ± 2.25	1.23 ± 0.71	1.11 ± 0.54	143.95 ± 94.84	6.50 ± 3.12
6	4.89 ± 2.40	1.44 ± 0.58	1.25 ± 0.53	165.31 ± 67.61	7.72 ± 3.04

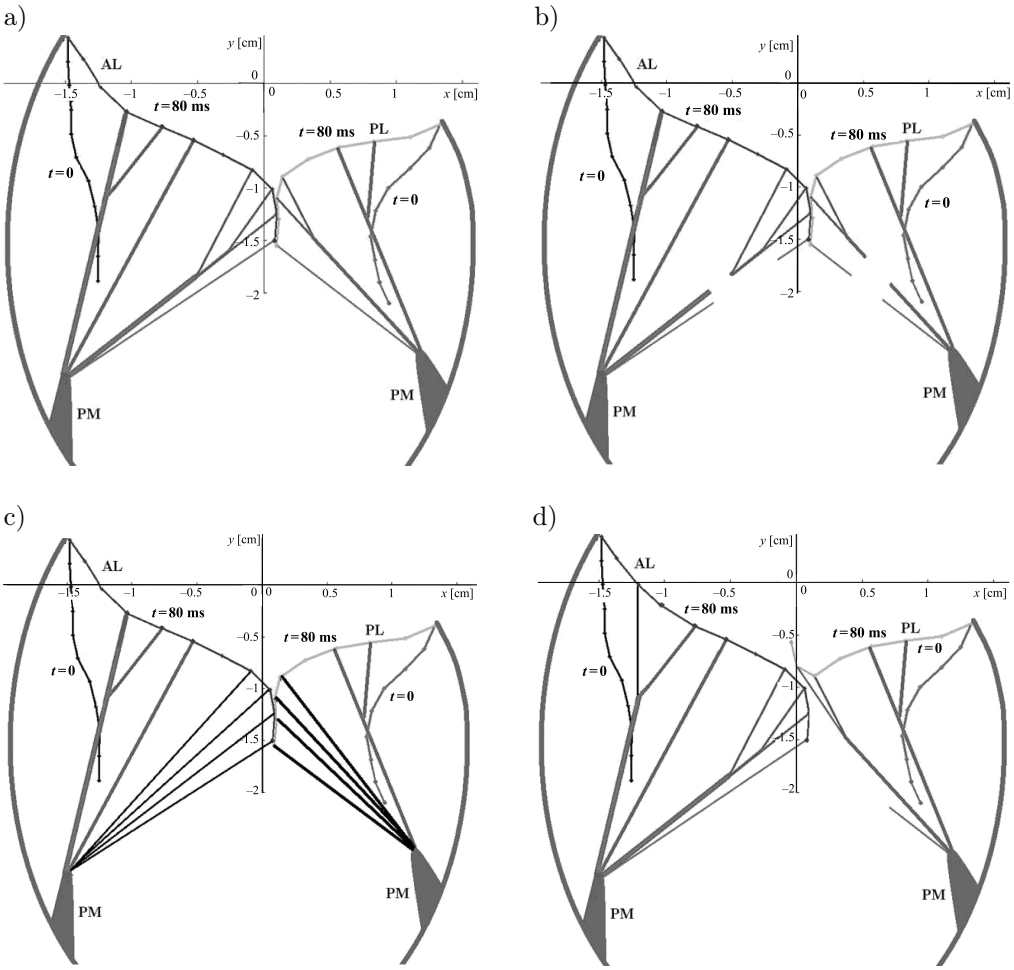

FIG. 12. The initial sample geometry of the MV (a), the case with broken marginal chordae (b), the virtually sewn neochordae (c), the corrected seagull defect and MV regurgitation (d).

the AL and PL extracted from the US images were used for the inverse problem solution and determination of the produced tensile forces to the critical values compatible to the tensile modules E^* for the human mitral valve chordae in healthy tissues and for some unhealthy tissues resulting from diseases [18–20]. Since the E^* values are strongly dependent on the cross-sectional area S of the chord, the experimental values used in the study are presented in Table 2.

Table 2. The tensile modules and tensile elongation for healthy and pathological human mitral valve chordae [18–20].

S [mm^2]	0.1–0.5	0.5–1.0	1.0–2.0	2.0–3.5
E^* [MPa] (healthy)	95 ± 20.2	80 ± 21.5	69 ± 14.3	64.8 ± 14.2
ΔL^* [%]	3.9 ± 1.9	7.5 ± 3.1	14.9 ± 4.4	19.8 ± 3.1
E^* [MPa] (disease)	18 ± 4.1	16.2 ± 4.4	14.1 ± 2.6	13.2 ± 2.2

The following problems were modelled on the initial MV geometry (Fig. 12a):

1. The broken marginal chorda in AL, PL and in both of them (Fig. 12b).
2. Sewn four neochordae from PTFE ($E = 10^8$ Pa) at AL and/or PL margin (Fig. 12c).
3. The central part of the basal chorda is cut to remove the so-called seagull effect (AL at $t = 80$ ms in Fig. 12a) and substituted with a pair of neochordae (AL in Fig. 12c).
4. MV regurgitation due to the broken marginal chordae with the virtual assignment of the locations for neochordae by a surgeon (PL in Fig. 12c).

For each case, the system of equation (3.1), (3.8), (3.9), (3.12) was composed for single and branched chordae. It was assumed that in the initial state ($t = 0$) all the chordae were at zero stress state ($\Delta L = 0$). The obtained system of nonlinear equations was solved using Newton's method with initial approximation given in Sec. 3. The method demonstrated very good accuracy and fast convergence. The accuracy was estimated by comparison of the numerical results obtained with $\eta_{1,2} = 0$ (see Sec. 3) to the computations on equivalent systems of linear elastic springs [21–23].

For the nonlinear viscoelastic parameters of the model, the equations were solved at a small time interval Δt. After computations of all the tensile forces, the corresponding displacements were computed, and the new location of the joints was determined. If elongation of the corresponding chorda exceeded $\Delta L =$ 1 cm, bigger values of the five material parameters were assigned to this chorda, according to/as in Table 1. When the computed tensile force $\mathbf{\Phi}_j^{(s)}$ exceeded the corresponding $E^*\Delta L$ value, the chorda was considered as broken, and the computations were stopped.

Some results of numerical computations are presented in Figs. 13a and 13b for the AL and PL accordingly. The horizontal lines correspond to conventional critical forces. When the tensile forces in the chordae exceed the critical values, the probability of the chorda rupture becomes high. The thin lines mark the average values for the healthy valve tissues, while at the age-related degenerative processes, some inflammatory states and other diseases lead to significant decrease of the critical forces (thick lines in Figs. 13a,b) [18–20]. The initial geometry of the AL is not healthy because of the seagull MV leaflet, and in the corresponding joint point the tensile forces slightly exceed the upper critical value (curve 1 in Fig. 13a). When one marginal chorda is broken, the stresses in the corresponding part of the leaflet become lower, but the neighbouring chorda becomes overloaded

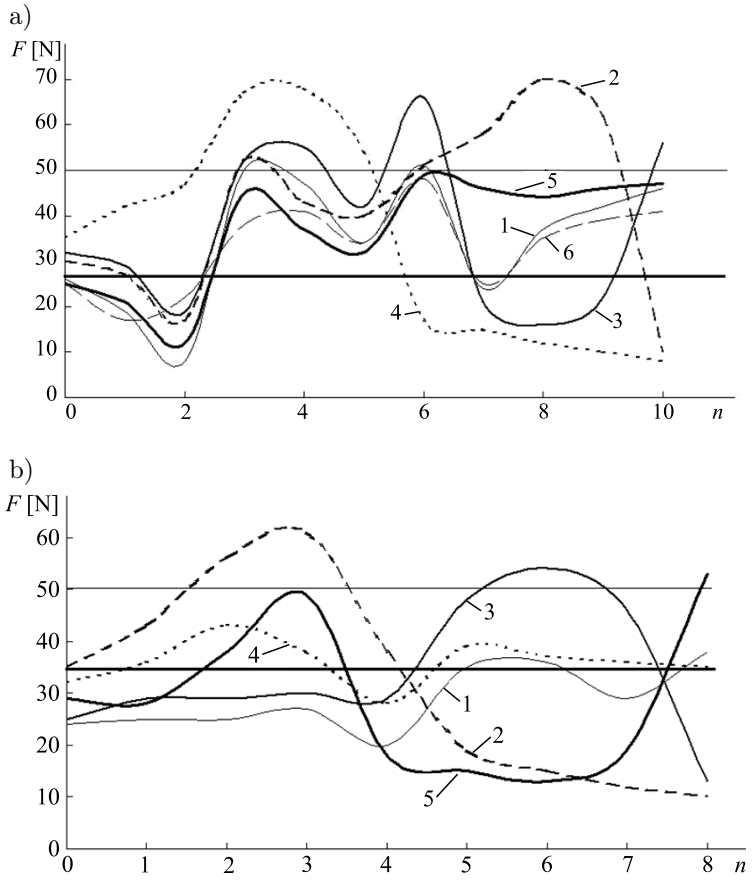

FIG. 13. Numerical results of the force distribution in the consecutive chords $n = 0, \ldots, 10$ of the AL; 1 – intact geometry (Fig. 12a), 2 – broken single margin chorda (Fig. 12b), 3 – branched chorda (Fig. 12b), 4 – broken both marginal chordae (Fig. 12b), 5 – sewn four neochordae, 6 – virtual surgical correction of the seagull shape; horizontal lines correspond to conventional critical forces for the healthy tissues (thin line) and affected (thick line).

(curves 2 in Figs. 13a,b). When the second (branched) chorda is ruptured, the first marginal chorda and the next healthy chorda become critically overloaded (curves 3 in Figs. 13a,b). When four neochordae from PTFE are sewn instead of the ruptured ones, the force distribution becomes more uniform along the margin of the leaflet, and the distribution in the basal part is also normalized (curves 5 in Figs. 13a,b). Incision of the short segment of the branched basal chord and the implantation, instead of it, of one or two neochordae decrease significantly the relatively high forces produced by the short thick segment (seagull shape). Unfortunately, when the tensile strength of the chordae is low due to diseases, implantation of neochordae does not provide a sufficient decrease in the tensile force distribution along the leaflets, and the risk of rupture remains high.

The computed regularities are in agreement with surgical observations and physical laws; the tested model is in good correspondence to the structural spring models and experimental measurements reported in the literature [15, 16]. Nevertheless, implementation of the developed model and approach into the virtual planning of surgery on the patient-specific geometry and valve dynamics into clinical practice needs more detailed investigations. Individual scatter in the material parameters of the viscoelastic soft tissues, the importance of the proper rheological model and residual strains, large variations in the parameters and geometry proper to healthy individuals and patients with different groups of diseases and ages are the most important topics for further studies. Besides, in the developed model, the generalized forces R_p produced by other factors such as shear forces and drag, hydrostatic pressure and blood flow streams and vortices were omitted. Their importance or insignificance must be shown which will be done in the further studies.

6. Summary

MV is composed of nonlinear viscoelastic materials and possesses complex geometry. The chordae attached to the margin and lower surfaces of the MV leaflets prevent the leaflets from the displacements outside of the left ventricle and provide unidirectional blood flow. When the chordae are overstretched, over distended or ruptured, different types of MV insufficiency develop. MV surgery includes among other procedures the neochordae sewn to replace the broken ones. Locations, lengths, and the stretch of the neochordae are chosen by intuition. First attempts of quantitative estimation of the outcomes of the surgery and virtual planning on the patient-specific models were based on the 2D and 3D FEM models which are time-consuming and need special research team for computations. Here a reasonable simple mechanical model of the MV dynamics based on the 2D HUS imaging of the valve dynamics was proposed. The leaflets in the side view are visible as smoothed polyline, while the papillary

muscles are seen as moving points. The coordinates of the digitized structures provided the boundary conditions for the marginal ends of the chordae fastened to the papillary muscles and leaflets. Then the location of the internal nodes of the chordae and the stress-strain distributions in the segments can be computed from Newton's second law. The problem is reduced to a set of non-linear algebraic equations for computations of coordinates of the internal nodes. Then the tensile forces in the chordae were computed from the rheological laws for elastic or viscoelastic chordae and compared to the critical values close to the ultimate tensile strength of the chordae of given thickness and age-related degradation level, inflammatory diseases or calcification. The model is simple and fast and can be useful not only for preliminary *in silico* planning of locations and lengths of the neochordae, but also for the real-time correcting computations during the surgery. Before the surgery, dozens of different neochordae locations could be computed and the best solution may be chosen. Further testing of the model is planned on the real clinical cases when the outcomes of the surgery after at least a year after the surgery are known.

Acknowledgment

The paper was presented at the 40th Solid Mechanics Conference held on 28.08–2.09.2016 in Warsaw (SolMech2016). The authors are kindly grateful to the participants of the conference for their important remarks and fruitful discussions.

References

1. Gefen A. [Ed.], *Patient-Specific Modeling in Tomorrow's Medicine*, Springer 2012.
2. Kerckhoffs R.C.P. [Ed.], *Patient-Specific Modeling of the Cardiovascular System. Technology-driven personalized medicine*, Springer, 2010.
3. Taylor C.A., Figueroa C.A., *Patient-specific modeling of cardiovascular mechanics*, Annual Reviews on Biomedical Engineering, **11**: 109–134, 2009.
4. Zhang W., Ayoub S., Liao J., Sacks M.S., *A meso-scale layer-specific structural constitutive model of the mitral heart valve leaflets*, Acta Biomaterialia, **32**: 238–255, 2016.
5. Feigenbaum H., Armstrong W.F., Ryan Th., *Feigenbaum's Echocardiography*, 6th ed., Philadelphia, Lippincott Williams & Wilkins, 2004.
6. Khalighi A.H., Drach A., ter Huurne F.M. *et al.*, *A comprehensive framework for the characterization of the complete mitral valve geometry for the development of a population-averaged model*, Lecture Notes in Computer Sciences, **9126**: 164–171, 2015.
7. Degandt A.A., Weber P.A., Saber H.A., Duran C.M.G., *Mitral valve basal chordae: comparative anatomy and terminology*, Annals of Thoracic Surgery, **84**: 1250–1255, 2007.
8. Song J.-M., Kim J.-J., Ha T.-Y. *et al.*, *Basal chordae sites on the mitral valve determine the severity of secondary mitral regurgitation*, Heart, **101**: 1024–1031, 2015.

9. Votta E., Caiani E., Veronesi F. *et al.*, *Mitral valve finite-element modelling from ultrasound data: a pilot study for a new approach to understand mitral function and clinical scenarios*, Philosophical Transactions of the Royal Society, Ser. A, **366**: 3411–3434, 2008.
10. Votta E., Le T.B., Stevanella M. *et al.*, *Toward patient-specific simulations of cardiac valves: State-of-the-art and future directions*, Journal of Biomechanics, **46**: 217–228, 2013.
11. Hammer P.E., Sacks M.S., del Nido P.J., Howe R.D., *Mass-spring vs. finite element models of anisotropic heart valves: speed and accuracy*, Proceedings of the ASME Summer Bioengineering Conference, Naples, Florida, USA, 2010.
12. Krishnamurthy G., Ennis D.B., Itoh A. *et al.*, *Material properties of the ovine mitral valve anterior leaflet in vivo from inverse finite element analysis*, American Journal of Physiology, **295**: H1141–H1149, 2008.
13. Gaidulis G., Kačianauskas R., Kizilova N., Romashov Y., *A mechanical model of heart valves with chords for in silico real time computations and cardio surgery planning*, 40th Solid Mechanics Conference, Warsaw, p. 157, 2016.
14. Romashov Y., Kizilova N., Gaidulis G., *Mathematical modeling of mitral valve dynamics: nonlinear vs linear models*, Proceedings of the 5th International Conference on Nonlinear Dynamics, Kharkov, Ukraine, pp. 208–215, 2016.
15. Rodriguez F., Langer F., Harrington K.B. *et al.*, *Importance of mitral valve second-order chordae for left ventricular geometry, wall thickening mechanics, and global systolic function*, Circulation, **110**: 115–122, 2004.
16. Bajona P., Zehr K.J., Liao J., Speziali G., *Tension measurement of artificial chordae tendinae implanted between the anterior mitral valve leaflet and the left ventricular apex; an in vitro study*, Innovations, **3**: 33–37, 2008.
17. Kochová P., Klepáček J., Hlubocky J. *et al.*, *Heart valve viscoelastic properties – a pilot study*, Applied and Computational Mechanics, **1**: 97–104, 2007.
18. Otto C.M., Bonow R.O. [Eds.], *Valvular heart disease: A companion to Braunwald's heart disease*, Saunders/Elsevier, Philadelphia, 2009.
19. Liao J., Vesely I., *A structural basis for the size-related mechanical properties of mitral valve chordae tendineae*, Journal of Biomechanics, **36**: 1125–1133, 2003.
20. Barber J.E., Ratliff N.B., Cosgrove D.M. 3rd, Griffin B.P., Vesely I., *Myxomatous mitral valve chordae. I: Mechanical properties*, The Journal of Heart Valve Diseases, **10**: 320–324, 2001.
21. Leet K.M., Uang C.-M., Gilbert A.M., *Fundamentals of structural analysis* (2nd ed.), McGraw-Hill, Boston, 2005.
22. Weggel D.C., Boyajian D.M., Chen Sh.-En., *Modelling structures as systems of springs*, World Transactions on Engineering and Technology Education, **6**: 169–172, 2007.
23. Olsson K.-G., Dahlblom O., *Structural mechanics: modelling and analysis of frames and trusses*, Wiley, 2016.

Received October 17, 2016; accepted version June 13, 2018.